

1 **Paper Title:** Estimating Reservoir Sedimentation Using Deep
2 Learning

3 **Authors:** Amanda L. Cox; Deanna Meyer; Alejandra Botero-Acosta; Vasit Sagan;
4 Ibrahim Demir; Marian Muste; Paul Boyd; and Chandra Pathak

5 **Affiliations:** WATER Institute (Cox, amanda.cox@slu.edu; Meyer, deanna.meyer@slu.edu;
6 Botero Acosta, alejandra.boteroacosta@slu.edu) and Taylor Geospatial Institute (Sagan,
7 vasit.sagan@slu.edu), Saint Louis University, St. Louis, Missouri, USA; Civil and
8 Environmental Engineering (Demir, ibrahim-demir@uiowa.edu) and IIHR- Hydroscience &
9 Engineering (Muste, marian-muste@uiowa.edu), University of Iowa, Iowa City, Iowa, USA; US
10 Army Corps of Engineers (Boyd, Paul.M.Boyd@usace.army.mil; Pathak,
11 Chandra.S.Pathak@usace.army.mil), Omaha, NE and Washington, DC, USA. (Correspondence
12 to Cox: amanda.cox@slu.edu).

13
14 This manuscript is an EarthArXiv preprint and has been accepted for publication in the peer-
15 reviewed ASCE Journal of Hydrologic Engineering. The final version of this manuscript may have
16 slightly different content. Copyright © 2024 ASCE. All rights reserved.

18 Estimating Reservoir Sedimentation Using Deep Learning

19 Amanda L. Cox, M.ASCE¹; Deanna Meyer¹; Alejandra Botero-Acosta¹; Vasit Sagan²; Ibrahim Demir³;

20 Marian Muste³; Paul Boyd⁴; and Chandra Pathak⁴

21 **Abstract:** Several reservoirs across the US are filling with sediment, which jeopardizes their
22 functionality and increases maintenance costs. The US Army Corps of Engineers (USACE)
23 developed the Reservoir Sedimentation Information (RSI) system to assess reservoir aggradation
24 and track dam operation suitability for water-resource management and dam safety. The RSI
25 dataset contains historical elevation-capacity data for approximately 400 dams (excluding
26 navigation structures) which correspond to less than 1% of dams across the US. Thus, there is a
27 critical need to develop methods for estimating reservoir sedimentation for unmonitored sites. The
28 goal of this project was to create a generalized method for estimating reservoir sedimentation rates
29 using reservoir design information and watershed data. To meet this objective, geospatial tools
30 were used to build a refined composite dataset to complement the RSI system's data with
31 precipitation and watershed characteristics. Nine deep learning models were then used on the
32 benchmark dataset to determine its accuracy at predicting capacity loss for the RSI reservoirs: four
33 supervised machine learning models, four deep neural network (DNN) models, and a multilinear
34 power regression model. A DNN model, containing a progressively increasing node and layer
35 construction, was deemed the most accurate, with R^2 values from its calibration and validation
36 datasets being 0.83 and 0.70, respectively. The best model was recalibrated over the entire dataset,
37 which showed greater accuracy on the prediction of RSI reservoir's capacity loss, with an R^2 of
38 0.81. This predictive model could be used to evaluate the capacity loss of unmonitored reservoirs,
39 forecast sedimentation rates under future climate conditions, and identify reservoirs with the
40 highest risk of losing functionality.

41 **Keywords:** Reservoir Sedimentation; Reservoir Capacity; Machine Learning.

42 **1. Introduction**

43 Dams and their associated reservoirs enable water storage, flood control, hydroelectric power
44 generation, and supply reliable water resources for various socio-economic needs. However,
45 reservoirs throughout the nation are slowly filling with sediment, diminishing their life cycle and
46 reducing their effectiveness, while increasing their cost of maintenance (Sholtes et al., 2018). The
47 immediate consequences of sediment retention in reservoirs are diminishing reservoir capacity,
48 creation of backwater flooding upstream, as well as impairing turbines of the structure (Morris and
49 Fan, 1998). The costs of remediating accumulated sediment in these structures may be exceedingly
50 expensive, with dam removal providing the greatest expense in dam decommissioning options
51 (U.S. Bureau of Reclamation, 2006).

52 Existing reservoir sedimentation models have been unable to analyze the intricate large-scale
53 temporal or spatial patterns of sedimentation due to a lack of available data required for model
54 calibration and validation. The typical data required for model construction include daily to yearly
55 hydrologic records, bathymetric reservoir details, and grain-size distribution of sediment (Ackers,
56 1988; Lajczak, 1996; Tarela and Menendez, 1999; Sundborg, 1992; Rowan et al., 2001). The most
57 valuable support for reservoir sedimentation model development in recent times has been provided
58 by Geographic Information System (GIS) tools that enables the addition of land use over large
59 scales to the hydrologic data (Verstraeten et al., 2003; Vorosmarty et al., 2003, Lehner et al., 2011).
60 However, GIS tools are relatively new hence their historical records are too short to refine
61 sedimentation modeling (Xu et al. 2019). This lack of temporal data in sedimentation modeling

62 diminishes the ability for proper model calibration, which has shown in sediment yield estimated
63 values to deviate considerably from measured sediment yield rates (Trimble, 1999).

64 The U.S. Army Corps of Engineers (USACE) oversees several dams and reservoirs across the
65 US, with many of them being under operation for more than 50 years (Pinson et al., 2016). The
66 aging of these USACE reservoirs makes them at greater risk for complications related to
67 sedimentation. Reservoir capacity surveys focused on US reservoir sedimentation trends indicate
68 that they could deplete by as much as 10%-35% of absolute water storage capacity (Randle et al.,
69 2019). These historical surveys are invaluable tools for identifying past and present regional
70 sedimentation trends, allowing for the evaluation of sediment aggradation and life expectancy of
71 individual reservoirs. These data are also relevant for developing effective reservoir management
72 strategies. Ensuing from the above, the USACE initiated the Enhancing Reservoir Sedimentation
73 Information for Climate Preparedness and Resilience (RSI) program to assess reservoir
74 aggradation and track dam operation suitability for water-resource management. However, since
75 the RSI dataset contains less than 1% of the US dams, developing methods for estimating reservoir
76 sedimentation at unmonitored sites is needed.

77 Machine learning as a tool for prediction and anomaly detection has developed rapidly over
78 the last couple of decades. Through several research studies, machine learning has been proven to
79 be successful at predicting streamflow, sediment transport, sediment deposition, and water-quality
80 characteristics as well as identifying data anomalies (Xiang and Demir, 2020; Azamathulla et al.,
81 2010; Choubin et al., 2017; Peterson et al., 2019; Xu et al., 2019; Peterson et al., 2020; Bhadra et
82 al., 2020; Hazarika et al., 2020). Due to the nonlinear behavior of sedimentation processes
83 influenced by various hydraulic flow factors, the use of machine learning has great potential for

84 constructing accurate reservoir capacity loss at unmonitored sites compared to alternative methods
85 (Adnan et al., 2019; Baniya et al., 2019). Machine learning utilizes the process of iteration and
86 probabilistic pattern detection to determine the relationship between input parameters and a
87 dependent variable (Geron, 2022). Prior to utilization of machine learning applications, the
88 sediment yield and sediment load, as well as estimated water pollutants was obtained through
89 various process-based modeling (Ayele et al., 2017; Zounemat-Kermani et al., 2019; Zounemat-
90 Kermani et al., 2020).

91 Machine learning modeling applied to reservoir sedimentation is not, however, infallible as
92 shown by the backpropagation networks used to assess sediment transfer occurring under differing
93 land use and agricultural practices (Abrahart and White, 2001). The valuable insights provided by
94 an artificial neural network model trained on 32 years of reservoir sedimentation data for one
95 reservoir (Jothiprakash and Garg, 2009) indicates that the availability of long-term data is critical
96 for trustful modeling outcome. It is however obvious that training machine learning requires not
97 only long-term data but also a great variety of reservoir in order to be more reliable and
98 generalizable.

99 The RSI system provides a good baseline resource for training data-driven models that could
100 be utilized for improved reservoir sedimentation estimation modeling through its combination of
101 temporal and spatial data spanning the contiguous US. The objective of this research was to create
102 a generalized deep learning method for estimating reservoir sedimentation using reservoir design
103 data and supplemental watershed information. To achieve this objective, the following tasks were
104 completed: 1) the RSI dataset was analyzed to determine capacity loss between consecutive
105 surveys, 2) supplemental hydrologic data were derived for each reservoir and set of consecutive

106 surveys (e.g., basin area and cumulative precipitation), 3) multiple deep learning algorithms were
107 applied using the composite dataset to create models to predict reservoir sedimentation, and 4)
108 model performances were analyzed and compared to identify a recommended model for industry
109 use. This prediction tool will allow the estimation of current conditions of unmonitored reservoirs
110 and forecast future sedimentation rates for reservoirs within the US.

111 **2. Composite RSI Dataset Development**

112 RSI information for 184 reservoirs was combined with supplementary watershed information
113 related to hydrologic and sedimentation processes to form the composite RSI dataset utilized in
114 this study. Each record of this dataset corresponded to two consecutive surveys conducted by the
115 USACE at that particular reservoir, and the capacity loss for each record was the difference in the
116 reservoir's capacity at the maximum pool elevation that was not characterized as a surcharge pool.

117 The RSI composite dataset incorporated data remotely compiled through publicly available
118 sources to ensure comprehensive watershed characteristics were associated with each recorded
119 reservoir's capacity loss. Utilization of raster datasets enabled the extraction of relevant hydrologic
120 data, which were identified and applied to their respective basins within the composite database.
121 These public databases provided data related to climatologic, topographic, and erosion processes
122 occurring across the associated watersheds, for each record within the composite dataset. Fig. 1
123 shows the features collected per each reservoir record, including the originally provided USACE
124 RSI system data, and the accessed public database. Reservoir features and basin characteristics
125 within the dataset were assumed constant over time for each reservoir. Thirty-two variables
126 compose the composite RSI dataset, including numerical variables (27), identifier variables (2),

127 categorical variables (2), and a date variable. Missing data records were replaced with the mean
128 for that specific variable.

129 The watershed centroid latitude and longitude values for each reservoir were extracted from
130 each basin's shapefile. The curve number (CN) and the erodibility values were computed for each
131 reservoir as the area-weighted average for its associated basin. The CN is the empirical hydrologic
132 parameter indicative of a catchment's runoff potential based on soil and land use characteristics
133 (USDA, 1986), while the erodibility index is an empirical measure of the inherent resistance of
134 geologic materials (soils and rocks) to erosion. The CN maps were based on national soil and
135 national land cover (NLCD) raster files (Viger and Bock, 2014; USGS, 2017). Utilizing USGS
136 characteristics for soil hydrologic groupings, and land use categorization, the CN values were
137 defined based on guidelines found in the Revised Universal Soil Loss Equation (RUSLE) for each
138 soil type (Renard, 1997). The average erodibility indices for sand (0.125), loam (0.325), and clay
139 (0.1) were used to create erodibility maps for each reservoir's basin based on the national soils
140 map (Viger and Bock, 2014). Additionally, the NLCD was used to compute the percent of forested
141 area within a reservoir's basin, with deciduous, evergreen, and mixed forest types consolidated
142 into one category for this study.

143 Google's Earth Engine facilitated the extraction and computation of variables from U.S.
144 Digital Elevation Models (DEMs) and monthly precipitation maps (US Geological Survey, 2017;
145 Gorelick et al., 2017). For this analysis, a 1/3rd arc-second DEM was utilized for calculating
146 features reliant on topographic information for the 184 reservoir basins within the composite
147 dataset. These features include hydraulic length, basin elevation, average slope, area, and relief,
148 which was defined as the difference between the maximum and minimum elevation. Based on

149 these calculations, the channel slope was estimated as the relationship of the relief divided by the
150 hydraulic length. A reservoir's initial trap efficiency (E) was calculated as a reservoir's initial
151 capacity in m³ (C), and a reservoir's drainage area in km² (A) shown in Eq. (1) (Brown, 1943).

$$152 \quad E = 1 - \frac{1}{1+(2.1 \times 10^{-4})C/A} \quad (\text{Eq. 1})$$

153 Further, precipitation data for each reservoir was found by analyzing 30 arc-second monthly
154 precipitation raster files (Daly *et al.*, 2015) that aligned with the database's time periods per each
155 set of consecutive surveys. Additionally, cumulative, maximum, mean, and median monthly
156 precipitations for each record were calculated. Further, the computation of normalized maximum
157 precipitation equaled the maximum precipitation divided by the mean monthly precipitation.

158 Since many dams were built upstream of RSI reservoirs, a batch analysis was employed to
159 include upstream dam heights, as well as the maximum, and normal storage of each reservoir
160 within the RSI composite dataset. This computation was conducted in two steps: 1) Utilize the
161 National Inventory of Dams (NID) dataset, composed of over 90,000 U.S. dams, to create an
162 annual time series of cumulative upstream dam height, and normal and maximum storage for each
163 RSI reservoir; 2) time average the upstream dam's variables, for the period of time comprising two
164 subsequent surveys for each RSI dataset record.

165 **2.1. Dataset Pre-Processing**

166 Due to natural processes, sustained or increases in reservoir capacity are not possible, unless
167 dredging or free-flow sediment flushing has been employed (Wang and Hu, 2009). Thus, a
168 reservoir's capacity will decrease over time. With this knowledge, the RSI composite dataset
169 records containing identical capacities, or an increased trend in capacity between a set of

170 consecutive surveys, were removed. Additionally, sets of consecutive surveys containing identical
171 survey data or dates were filtered out.

172 A log transformation (Brakstad, 1992; Emmerson *et al.*, 1997), was applied to the numerical
173 variables of the RSI composite dataset to remove the impact of the difference in orders of
174 magnitude. The following provides the equation for the log transformation:

$$175 \quad x_{l_i} = \text{sgn}[\ln(|x_i| + 1)] \quad \text{Eq. (2)}$$

176 where x_i is the original data value; x_{l_i} is the log-transformed value; i is the number of observations;
177 and the *sgn* function multiplies the value by either a value of one if x_i is a positive value or a value
178 of negative one if x_i is a negative value. Additionally, a minimum-maximum (min-max)
179 normalization (Goyal *et al.*, 2014; Patro and Sahu, 2015) of the numerical variables was conducted
180 using the following equation:

$$181 \quad x_{lm_i} = 0.7 \left(\frac{x_{l_i} - x_{l_{min}}}{x_{l_{max}} - x_{l_{min}}} \right) + 0.15 \quad \text{Eq. (3)}$$

182 where x_{lm_i} is the log-transformed and min-max normalized value; x_i is the original data value; x_{l_i}
183 is the log-transformed value; where $x_{l_{min}}$ is the minimum value of the x_l dataset; $x_{l_{max}}$ is the
184 maximum value of the x_l dataset. This results in a linear scaling with values ranging from 0.15 to
185 0.85. The min-max normalization of data fits the data in a pre-defined range keeping the
186 relationships from the original data unchanged (Patro and Sahu, 2015).

187 Depending on the performance of models, standard scaling was applied in lieu of the min-max
188 normalization. This normalization method minimizes the number of parameters that appear
189 constant across the dataset, which can affect model performance. Standard scaling centers the
190 dataset values around the mean with a unit of standard deviation (Cao *et al.*, 2016). The following
191 equation details the standard scaling calculations:

192
$$x_{ls_i} = \frac{x_{l_i} - \mu}{\sigma} \quad \text{Eq. (4)}$$

193 where x_{ls_i} is the log-transformed scaled value; μ is the mean of the x_{l_i} dataset; and σ is the standard
194 deviation of the x_{l_i} dataset.

195 **3. Methods**

196 The dataset compiled for the RSI reservoir sites consisted of variables relevant to sedimentation
197 and hydrologic processes. Transformation and scaling of the dataset were performed to diminish
198 bias and skew of the variables' distribution. A feature importance analysis was conducted to
199 analyze the sensitivity of variables detrimental to model performance, which resulted in the
200 creation of a dataset with decreased variable size. The original and the feature-importance-derived
201 datasets were used to develop and evaluate capacity loss prediction models. Both sets of data were
202 examined in each iteration of the statistical or machine learning method. For all models analyzed,
203 a 70/30 split of the dataset was applied for the training and testing of the models, respectively.

204 The first statistical model used was the Ordinary Least Squares (OLS) multilinear regression
205 model. The second analysis consisted of four supervised machine learning regression models:
206 Support Vector Machine (SVM), Random Forest (RFR), Decision Tree (DTR), and Partial Least
207 Squares (PLS). The third analysis used deep neural network (DNN) models. In the DNN model
208 survey, four base DNN architectures were analyzed.

209 A data anomaly detection was performed to reduce erroneous data within the composite
210 dataset. This included anomaly removals utilizing Autonomous Anomaly Detection (AAD)
211 (Angelov et al., 2016; Gu and Angelov, 2017), which flagged 18 records corresponding to 15
212 reservoirs, and the Kolmogorov-Smirnov and Efron (KSE) outlier detection method (Jirachan and

213 Priomsopa, 2015), which flagged 15 records corresponding to 10 reservoirs. Removal of
214 anomalous data from data used in model development varied by model based on performance.

215 Lastly, seven metrics were used to compare all created models. The following performance
216 parameters were quantified for evaluation and goodness-of-fit analysis of the statistical models:
217 coefficient of determination (R^2), Mean Absolute Percent Error (MAPE), Root Mean Square Error
218 (RMSE), and Relative Root Mean Square Error (RRMSE). The remaining three parameters
219 included the Percent Bias (PBias), the ratio of root mean squared error to standard deviation of
220 measured data (RSR), and the Pearson Correlation Coefficient (r), to help analyze the models'
221 overall accuracy outside the limitations of correlation-based measures (Legates & McCabe, 1999).
222 Respectively, these three metrics were used to quantify each model's overestimation or
223 underestimation, normalization to error index evaluation in model performance (Moraisi et al.,
224 2007), and uncover the degree of linear association between calibrated and observed values of the
225 model (Taylor, 1990; Adler and Parmyryd, 2010). Collectively, watershed model performance
226 metrics can be considered satisfactory if $R^2 > 0.5$, PBias + 55%, RSR < 0.7, and $r > 0.5$ (Moriasi
227 et al., 2007; Ayele et al., 2017).

228 ***3.1. Feature Correlation and Recursive Feature Elimination (RFE)***

229 A Spearman's rank correlation calculation was performed to measure the monotonic relationship
230 across predictor variables. Ranging from -1 to 1, the Spearman's calculated coefficient gauges
231 whether two features are correlated, with -1 being negatively correlated and 1 being positively
232 correlated (Bon-Gang, 2018). Determining these relationships between the predictor variables was
233 necessary to investigate potential collinearity shared across the composite dataset, and if removal

234 of features could improve ensuing model performance. The general criterion for modeling a
235 regression analysis is a minimum of 10 to 20 samples per predictor variable (Austin and
236 Steyerberg, 2015).

237 To observe if reducing the number of predictor variables in the composite dataset improved
238 results, a *Recursive Feature Elimination* (RFE) algorithm was performed from which an
239 alternative dataset was developed. Utilizing optimized random forest model parameters, the RFE
240 was used to establish the optimal amount of predictor variables for this new RFE-determined
241 dataset. The RFE algorithm assigns weights to features based on model performance. The
242 significance of this algorithm is its allowance to choose the number of features desired in the
243 reduced dataset, and its theoretical improvement within statistical modeling through its removal
244 of collinear features. The presence of numerous collinear features can lead to overfitting when
245 analyzing the prediction of dependent variables through machine learning models (Harrell, 2001).

246 **3.2. Ordinary Least Squares Multilinear Regression**

247 The Ordinary Least Squares (OLS) multilinear regression model is used for relational analysis
248 between one or more variables. The method corresponds to the minimization of the sum of the
249 square error difference between the observed and predicted values of the target variable, as it fits
250 an assumed linear relationship between the explanatory variables (Zdaniuk, 2014). The OLS
251 regression formula to compute capacity loss, y_i :

$$252 \quad y_i = \beta_0 + \beta_1 x_{i_1} + \beta_2 x_{i_2} + \dots + \beta_p x_{i_p} + \epsilon \quad \text{Eq. (6)}$$

253 where i is the number of observations, y_i is the dependent variable, x_{i_j} are the explanatory
254 variables, β_0 is the y-intercept or constant term of the equation, β_p is the slope coefficients for
255 each explanatory variable, and ϵ is the residuals of the model (Alexopoulos, 2010). Standard

256 scaling was used to evaluate the magnitude of influence each predictor variable had on the target
257 variable. Imperial system units were used for the OLS analysis and due to regression model
258 complexity, all International System of Units (SI) values must be converted to imperial units for
259 application. When using the OLS method with metric units, the SI value of each input parameter
260 should be multiplied by the corresponding metric unit conversion factor listed in Table 1 prior to
261 the log-transformation in Eq. 2. Similarly, the capacity loss term, y_i , computed from Eq. 6 is in
262 acre-ft and needs to be multiple by 1,233 for conversion to m^3 .

263 **3.3. Supervised Machine Learning**

264 Supervised machine learning is the application of algorithms capable of producing generalities in
265 patterns via the use of externally supplied data to predict future patterns and instances (Singh *et*
266 *al.*, 2016). Several types of supervised machine learning algorithms exist, but for this analysis
267 SVM (Noble, 2006), RFR (Breiman, 2001), DTR (Bashar *et al.*, 2019), and PLS (Manikanta *et al.*,
268 2015) regression algorithms were utilized. Each algorithm has advantages and disadvantages when
269 applied to a unique dataset; thus, implementation of these four enabled comprehensive analysis of
270 supervised learners on the composite and RFE datasets. Additionally, each supervised learner used
271 a pipeline of several intermediary steps, that chained a sequence of estimators for optimization and
272 cross-validation of model performance. These steps included a principal component analysis and
273 standard scaling. These optimizing components were refined by automated selection of each
274 model's hyperparameters resulting in the highest performing variation of the supervised model.

275 **3.4. Deep Neural Network (DNN)**

276 A DNN is an organized collection of neurons sequenced into multiple layers for determining
277 modeled predictions. The neurons receive input from the initial dataset if they reside within the

278 first layer of the DNN, or from input from activated neurons from previous layers if residing within
279 a subsequent layer. The activations of the neurons occur based on a calculation of the weighted
280 sums from that input followed by a nonlinear activation (Montavon *et al.*, 2018). In the case of
281 this analysis, the Rectified Linear (ReL) activation function was used. All nodes that consist of
282 this activation function are considered rectified linear activation units (ReLU), whose development
283 was a milestone in the evolution of deep learning (Goodfellow *et al.*, 2016). Deep learning (DL)
284 studies have gained significant momentum with the availability of computational resources,
285 benchmark datasets (Demir *et al.*, 2022; Sit *et al.*, 2021a), and the popularity of DL algorithms in
286 many data analysis tasks in water resources and hydrology including streamflow forecasting (Sit
287 *et al.*, 2022b), culvert sedimentation (Xu *et al.*, 2019), data augmentation (Demiray *et al.*, 2021),
288 and image synthesis (Gautam *et al.*, 2022).

289 For this analysis, four DNN architectures were utilized, and the models were optimized to
290 minimize the mean absolute error (MAE). The basis of the first DNN architecture was used in the
291 research of Maimaitijiang *et al.* (2020), which contained a GIS and remotely sensed dataset.
292 Named DNN-F1, it incorporated a DNN node structure that continually increased in complexity
293 per each layer. The minimum number of nodes residing within the initial layer was 64, and the
294 maximum number of nodes retained within the final layering was 1024. For the purposes of this
295 study, this first progressively increasing DNN (termed DNN_{PI1}), will be the base DNN used to
296 compare further DNN architectures. The second DNN architecture was aimed at analyzing if
297 information bottlenecking could improve the initial DNN. The bottlenecking method aims to
298 balance improved accuracy through decreasing complexity (Tishby *et al.*, 2000; Hecht and Tishby,
299 2005). This version of the DNN reverses the initial architecture to become a progressively

300 decreasing DNN (termed DNN_{PD1}), which results in its initial layer containing a node network of
301 1024, and its final layer containing a node network of 64. Schematics of the DNN_{PI1} and DNN_{PD1}
302 architectures are shown in Fig. 2.

303 Two simplified DNN structures were also evaluated to determine their performance compared
304 to the complex DNN_{PI1} and DNN_{PD1} structures: a second progressively increasing DNN (termed
305 DNN_{PI2}) and a second progressively decreasing DNN (termed DNN_{PD2}). Detailed node
306 architectures for these simpler DNNs are shown in Fig. 3. The DNN_{PI2} and DNN_{PD2} structures
307 have half the number of layers as the DNN_{PI1} and DNN_{PD1} , and fewer nodes associated with each
308 of their layers. The DNN_{PI2} structure contains an initial neural structure that starts with 8 nodes
309 and increases to 32 in its final layer. The DNN_{PD2} structure is the reversed iteration of the DNN_{PI2} .

310 **4. Results and Discussion**

311 **4.1. Feature Importance Analysis**

312 To identify collinearity or monotonic relationships between features, a Spearman's rank
313 coefficient matrix analysis was performed. Values closest to 1 or -1 were respectively deemed
314 highly positively or negatively correlated. The digital elevation model (DEM) parameters showed
315 a significant positive correlation with each other, as well as basin relief with values ranging from
316 0.57 to 0.92. Alternatively, the DEM parameters appear negatively correlated to the monthly
317 precipitation parameters with values of -0.54 to -0.66. This analysis signifies that the compiled
318 features within the dataset contain redundancies.

319 **4.2. Recursive Feature Elimination (RFE)**

320 The Recursive Feature Elimination (RFE) algorithm was applied to reduce potentially redundant
321 features and further optimize the performance of the predictive models. The composite dataset

322 consisted of 467 samples with 27 predictor variables. Thus, the dataset had a ratio of approximately
323 17 samples per predictor variable within the dataset. When reducing composite dataset features,
324 the RFE conducts its model accuracy performance based on R^2 values, with 1.00 being the highest
325 accuracy score possible. The RFE results showed that twelve predictor variables retained an R^2
326 value of between 0.78 – 0.80. With less than twelve variables, the accuracy scored less than or
327 equal to 0.77. Thus, the twelve predictor variables listed in Table 1 were optimal in minimizing
328 the composite dataset to a sample-to-feature ratio of approximately 38. This new RFE dataset was
329 used in subsequent models and the results were compared to the entire composite dataset. Standard
330 scaling was used to help further analyze the magnitude of influence each predictor variable had on
331 the target variable, within the OLS equation.

332 The inclusion of basin relief, hydraulic length, and the channel slope features within the RFE
333 dataset, may be seen as still maintaining excessive collinear features. However, due to the
334 logarithmic transformation and normalizations performed on the data, the feature of channel slope,
335 which is derived from hydraulic length and basin relief, is mathematically unique in terms of
336 providing a predictive value within the model's equation.

337 Three features are indicators of drainage basin size: basin area, hydraulic length, and basin
338 relief. The basin area model coefficient of 0.548 indicates that area is the dominant feature related
339 to basin size. Based on the Spearman correlation analysis, both basin length and relief are
340 positively correlated with capacity loss. However, both the length and relief coefficients are
341 inversely related to the predictive variable (i.e., capacity loss) suggesting their model contribution
342 is an adjustment on the basin area influence.

343 All models developed using the RFE dataset resulted in improved performance compared to
 344 models from the entire composite dataset. Due to the large number of models generated, only the
 345 RFE results are reported.

346 **4.3. OLS Regression Model**

347 The log-transformed RFE dataset with no anomalies removed was found to produce the best OLS
 348 model performance. The observed versus predicted training and testing results for the OLS model
 349 are shown in Fig. 4. Following the training/testing analysis, the OLS model was calibrated using
 350 the full dataset to provide the overall best-fit equation. Figure 4 also shows the observed versus
 351 predicted values for the calibrated OLS model which had an R^2 value of 0.40 and a MAPE of
 352 195%. Equation (7) provides the OLS prediction equation based on the coefficient values and
 353 constant terms derived from the calibrated OLS model results:

$$\begin{aligned}
 354 \quad y_{OLS_l} = & -9.71 + 0.548x_{l_1}U_1 + 0.476x_{l_2}U_2 + 0.383x_{l_3}U_3 \\
 355 & -0.169x_{l_4}U_4 + 0.561x_{l_5}U_5 + 1.59x_{l_6}U_6 \\
 356 & -0.0460x_{l_7}U_7 + 0.0250x_{l_8}U_8 - 0.0249x_{l_9}U_9 \\
 357 & +1.87x_{l_{10}}U_{10} + 0.188x_{l_{11}}U_{11} + 0.0588x_{l_{12}}U_{12} \quad \text{Eq. (7)}
 \end{aligned}$$

358 where y_{OLS_l} is the log-transformed predicted capacity; x_{l_p} are the log-transformed predictor
 359 variables; U_p is the metric unit conversion factor; and the numeric subscript p on the x_l and U
 360 terms denotes the variable index (Table 1). To obtain the predicted capacity loss value, the model
 361 predicted value (y_{OLS}) needs to be un-transformed using Eq.(8):

$$362 \quad y_{OLS} = (e^{y_{OLS_l}} - 1) * 1233 \quad \text{Eq. (8)}$$

363 **4.4. Supervised Machine Learning**

364 The best performing supervised machine learning model was identified based on the satisfactory
365 statistical metrics defined by Moriasi et al., 2007. Nearly all the supervised machine learning
366 models had optimal performance when using the log-transformed normalized RFE dataset with
367 the KSE anomalies removed. The supervised machine learning results presented within this report
368 were all developed using this dataset. A comparison between the supervised machine learning
369 methods showed that the RFR had the most accuracy, in terms of predictive performance, when
370 trained and tested on the respective data. With a training set R^2 of 0.61 and a testing set R^2 of 0.57,
371 the model shows precision in model fitness when comparing the predicted versus observed values
372 of capacity loss. Tables 2 and 3 show the performance metrics of the training and testing results
373 for this model. Notably, there is a significant increase in MAPE on the testing dataset's forecasting
374 accuracy. This signifies that the model training results are overestimating the model's
375 performance, regardless of the relatively high R^2 value present on the testing dataset.

376 **4.5. DNN Analysis**

377 All the DNN models had optimal performance when using the log-transformed normalized RFE
378 dataset with the KSE anomalies removed. The DNN results presented for this study were
379 developed using this dataset. The complex DNNs had significantly better accuracy based on the
380 MAPE and R^2 values. The DNN_{PII} was identified as the best DNN model variation based on
381 maximizing the R^2 and minimizing the RRMSE. Training and testing results for this DNN model
382 are shown in Table 3. The DNN_{PII} had training and testing R^2 values of 0.83 and 0.70, respectively.
383 This makes the DNN_{PII} the best fitting model in terms of performance. The RRMSE values of the
384 DNN_{PII} were the lowest RRMSE values compared across all analyzed machine learning models.

385 However, the MAPE and RRMSE values showed a relatively large percentage increase between
386 training and testing, meaning there may be underlying forecasting inaccuracies.

387 **4.6. Comparison of Models**

388 A comparison of the supervised machine learning, DNN, and OLS models is shown in Fig. 4;
389 model summary statistics for the untransformed model data are provided in Table 2 and Table
390 **3Table 3**. All models were developed using the transformed data, but the prediction variable of
391 interest is the capacity loss (i.e., not the log-transformed capacity loss). Thus, untransformed
392 statistics were used to assess model performance and their values are reported on all observed
393 versus predicted plots. Further, results shown are for the RFE dataset (feature variables listed in
394 Table 1) as the RFE dataset performed better than the original composite dataset for all models
395 analyzed. Except for RFR, the supervised machine learning methods resulted in abnormal
396 predictive performance. However, the RFR, and the more complex DNNs, showed promising
397 results in terms of learning and predicting capacity loss. Overall, the best tested model
398 performance, based on R^2 and RRMSE, was the DNN_{PI1} with an untransformed R^2 value of 0.70
399 and an untransformed RRMSE of 135%.

400 The RRMSE values measured across all models, as they relate to the OLS RRMSE value are
401 shown in Fig. 5. The OLS method of prediction compared respectably when set side by side with
402 more computationally complex machine learning models in terms of R^2 and MAPE. However, the
403 more complex models did result in considerably lower RRMSE values, compared to the OLS
404 method.

405 In Table 4, based on the R^2 , PBias, RSR, and r metrics, DNN_{PI1} further proved as the best
406 model that exhibited satisfactory performance for all training and testing metrics, for which the

407 cumulative capacity loss, observed versus simulated capacity loss, and capacity loss data series are
408 presented in Fig. 6. However, notably, the DNN_{PII} model appears more accurate at estimating
409 lower levels of cumulative capacity loss on the testing data until it reaches records with capacity
410 loss values of greater than $1.23 \times 10^8 \text{ m}^3$.

411 Consequently, the model recommended for capacity loss prediction is a calibrated DNN_{PII}
412 model. The calibrated DNN_{PII} was established through training the original best performing
413 DNN_{PII} model on the entire RFE dataset. This was conducted to overcome potential inaccuracies
414 associated with the limited records available, which is the case with the current RSI dataset. For
415 this calibrated model, the R^2 increased to 0.81 and the MAPE value decreased to 38%, as shown
416 in Table 3. This shows significant improvement in terms of forecasting accuracy, compared to all
417 models. Figure 4 illustrates the observed versus predicted capacity loss values for the calibrated
418 DNN_{PII}. Thus, the model successfully learned on the training dataset, producing satisfactory
419 performance metrics. However, high accuracy determinations for larger amounts of capacity loss
420 still appear limited.

421 **5. Conclusions**

422 A composite dataset was developed which included capacity loss data obtained from RSI system
423 records and 29 supplemental parameters derived from publicly available databases. The composite
424 dataset included 184 reservoirs, 799 surveys, and 615 sets of consecutive surveys for evaluating
425 capacity loss. The study demonstrated that prediction models containing supplemental data inputs
426 estimate reservoir capacity loss (acre-ft) with satisfactory R^2 , PBias, RSR, and r values as defined
427 in Moriasi et al., 2007. Of the nine predictive models, the progressively increasing deep neural
428 network (DNN_{PII}) had the best predictive performance with model training and testing R^2 values

429 of 0.83 and 0.70, respectively; and training and testing MAPE of 87% and 295%, respectively.
430 Notably, the DNN_{PII} had higher accuracy at predicting capacity loss values lower than 1.23×10^8
431 m^3 . The DNN_{PII} model was recalibrated over the entire dataset with resulting R^2 and mean absolute
432 percent error (MAPE) values of 0.81 and 48%, respectively. Accordingly, the DNN_{PII} is the most
433 promising model for estimating reservoir capacity losses using watershed and historical
434 precipitation data which enables the identification of vulnerable reservoirs within the US. Further,
435 the DNN_{PII} model can be used to forecast reservoir sedimentation rates under possible future
436 climate scenarios which allows for the development of proactive management plans.

437 **6. Acknowledgements**

438
439 This research was supported by the U.S. National Science Foundation (Award # 1948940) and the
440 WATER Institute at Saint Louis University.

441 **7. References**

- 442 Abrahart, R. J., & White, S. M. (2001). Modelling sediment transfer in Malawi: comparing
443 backpropagation neural network solutions against a multiple linear regression benchmark
444 using small datasets. *Physics and Chemistry of the Earth, Part B: Hydrology, Oceans and*
445 *Atmosphere*, 26(1), 19-24.
- 446 Adler, J., & Parmryd, I. (2010). Quantifying colocalization by correlation: the Pearson
447 correlation coefficient is superior to the Mander's overlap coefficient. *Cytometry Part A*,
448 77(8), 733-742.
- 449 Adnan, M. S., Dewan, A., Zannat, K. E., & Abdullah, A. M. (2019). The use of watershed
450 geomorphic data in flash flood susceptibility zoning: a case study of the Karnaphuli and
451 Sangu river basins of Bangladesh. *Natural Hazards*, 99, 425-448.

- 452 Alexopoulos, E. C. (2010). Introduction to multivariate regression analysis. *Hippokratia*, 14(1),
453 23-28.
- 454 Austin, P. C., & Steyerberg, E. C. (2015). The number of subjects per variable required in linear
455 regression analyses. *Journal of Clinical Epidemiology*, 68(6), 627-636.
456 doi:<http://dx.doi.org/10.1016/j.jclinepi.2014.12.014>
- 457 Ayele, G. T., Teshale, E. Z., Yu, B., Rutherford, I. D., & Jeong, J. (2017). Streamflow and
458 sediment yield prediction for watershed prioritization in the Upper Blue Nile River Basin.
459 *Water*, 9(10), 782.
- 460 Baniya, B., Tang, Q., Xu, X., Haile, G. G., & Chhipi-Shrestha, G. (2019). Spatial and temporal
461 variation of drought based on satellite derived vegetation condition index in Nepal from
462 1982-2015. *Sensors*, 19(2), 430.
- 463 Bashar, S. S., Miah, M. S., Zaidul Karim, A., & Al Mahmud, M. (2019). Extraction of Heart
464 Rate from PPG signal: A Machine Learning Approach using Decision Tree Regression
465 Algorithm. *4th International Conference on Electrical Information Communication
466 Technology (EICT)*, (pp. 1-6). Khulna, Bangladesh.
- 467 Bon-Gang, H. (2018). *Performance and Improvement of Green Construction Projects:
468 Management Strategies and Innovations*. Butterworth-Heinemann.
- 469 Brakstad, F. (1992). A Comprehensive Pollution Survey of Polychlorinated Dibenzo-P-Dioxins
470 and Dibenzofurans by Means of Principal Component Analysis and Partial Least-Squares
471 Regression. *Chemosphere*, 24(12), 1885-1903.
- 472 Breiman, L. (2001). Random Forests. *Machine Learning*, 45, 5-32.
473 doi:<http://dx.doi.org/10.1023/A:1010933404324>

474 Brown, C. B. (1943). Discussion in Sedimentation in Reservoirs. (B. J. Witzig, Ed.) *Transactions*
475 *of the American Society of Civil Engineers*, 109, 1047-1106.

476 Cao, X. H., Stojkovic, I., & Obradovic, Z. (2016). A robust data scaling algorithm to improve
477 classification accuracies in biomedical data. *BMC Bioinformatics*, 17(1), 1-10.

478 Choubin, B. H., Darabi, H., Rahmati, O., Sajedi-Hosseini, F., & Klove, B. (2017). River
479 suspended sediment modelling using the CART Model: A comparative study of machine
480 learning techniques. *Science of The Total Environment*, 615:272-281.

481 Daly, C., Smith, J. I., & Olson, K. V. (2015). Mapping atmospheric moisture climatologies
482 across the conterminous United States. *PloS One*, 10(10), e0141140.

483 Demiray, B. Z., Sit, M., & Demir, I. (2021). D-SRGAN: DEM super-resolution with generative
484 adversarial networks. *SN Computer Science*, 2(1), 1-11.

485 Emmerson, R. H., O'Reilly-Wiese, S., Macleod, C., & Lester, J. (1997). A multivariate
486 assessment of metal distribution in inter-tidal sediments of the Blackwater Estuary, UK.
487 *Marine Pollution Bulletin*, 34(11), 960-968.

488 Gautam, A., Sit, M., & Demir, I. (2022). Realistic river image synthesis using deep generative
489 adversarial networks. *Frontiers in Water*, 4.

490 Goodfellow, I., Bengio, Y., & Courville, A. (2016). *Deep Learning*. MIT Press.

491 Gorelick, N., Hancher, M., Dixon, M., Ilyushchenko, S., Thau, D., & Moore, R. (2017). Google
492 Earth Engine: Planetary-scale geospatial analysis for everyone. *Remote Sensing of*
493 *Environment*, 202, 18-27.

494 Goyal, H., Sandeep, D., Vanu, R., Pokuri, R., Kathula, S., & Battula, N. (2014). Normalization
495 of Data in Data Mining. *International Journal of Software and Web Sciences*, 14, 32-33.

496 Harrell, F. E. (2001). *Regression Modeling Strategies: With Application to Linear Models,*
497 *Logistic Regression, and Survival Analysis.* Springer.

498 Hazarika, B. B., Gupta, D., & Berlin, M. (2020). Modeling suspended sediment load in a river
499 using extreme learning machine and twin support vector regression with wavelet
500 conjunction. *Environmental Earth Sciences, 79*:1-15.

501 Hecht, R. M., & Tishby, N. (2005). Extraction of relevant speech features using the information
502 bottleneck method. *Interspeech.*

503 Jothiprakash, V., & Garg, V. (2009). Reservoir sedimentation estimation using artificial neural
504 network. *Journal of Hydrologic Engineering, 14*(9), 1035-1040.

505 Legates, D. R., & McCabe Jr., G. J. (1999). Evaluating the use of "goodness-of-fit" measures in
506 hydrologic and hydroclimatic model validation. *Water Resources Research, 35*(1), 233-
507 241.

508 Lehner, B., Liermann, C. R., Revenga, C., Vorosmarty, C., Fekete, B., Crouzet, P., . . . Wissler,
509 D. (2011). High-resolution mapping of the world's reservoirs and dams for sustainable
510 river-flow management. *Frontiers in Ecology and the Environment, 9*(9), 494-502.

511 Maimaitijiang, M., Sagan, V., Sidike, P., Hartling, S., Esposito, F., & Fritschi, F. (2020).
512 Soybean yield prediction from UAV using multimodal data fusion and deep learning.
513 *Remote Sensing of Environment, 237*, 111599.

514 Manikanta, C., & Mamatha Jadav, V. (2015). Evaluation of modified PLS regression method to
515 fill the missing values in training dataset. *International Conference on Smart Sensors and*
516 *Systems (IC-SSS)*, (pp. 1-5).

517 Montavon, G., Wojciech, S., & Klaus-Robert, M. (2018). Methods for interpreting and

518 understanding deep neural networks. *Digital Signal Processing*, 73, 1-15.

519 Moriasi, D. N., Arnold, J., Van Liew, M., Bingner, R., Harmel, R., & Veith, T. (2007). Model
520 evaluation guidelines for systematic quantification of accuracy in watershed simulations.
521 *Transactions of the ASABE*, 50(3), 885-900.

522 Morris, G., & Fan, J. (1998). *Reservoir Sedimentation Handbook: Design and Management of*
523 *Dams, Reservoirs, and Watershed for Sustainable Use*. New York: McGraw-Hill.

524 Noble, W. S. (2006). *What is a support vector machine?* Retrieved 2021, from Nature.com:
525 [https://www.ifi.uzh.ch/dam/jcr:00000000-7f84-9c3b-ffff-](https://www.ifi.uzh.ch/dam/jcr:00000000-7f84-9c3b-ffff-ffffc550ec57/what_is_a_support_vector_machine.pdf)
526 [ffffc550ec57/what_is_a_support_vector_machine.pdf](https://www.ifi.uzh.ch/dam/jcr:00000000-7f84-9c3b-ffff-ffffc550ec57/what_is_a_support_vector_machine.pdf)

527 Patro, S., & Sahu, K. (2015). Normalization: A Preprocessing Stage. *ArXiv*, *abs/1503.06462*.

528 Pinson, A., Baker, B., Boyd, P., Grandpre, R., White, K., & Jonas, M. (2016, 05). U.S. Army
529 Corps of Engineers Reservoir Sedimentation in the Context of Climate Change. *Civil*
530 *Works Technical Report (CWTS) 2016-05*.

531 Randle, T., Morris, G., Tullos, D., Weirich, F., Kondolf, G., Moriasi, D., & Wegner, D. (2021).
532 Sustaining United States reservoir storage capacity: Need for a new paradigm. *Journal of*
533 *Hydrology*, 602, 126686.

534 Renard, K. G. (1997). *Predicting soil erosion by water: a guide to conservation planning with*
535 *the Revised Universal Soil Loss Equation (RUSLE)*. United States Government Printing.

536 Sholtes, J., Ubing, C., Randle, T., Fripp, J., Cenderelli, D., & Baird, D. (2018). Managing
537 infrastructure in the stream environment. *Journal of the American Water Resources*
538 *Association*, 54(6), 1172-1184.

539 Singh, A., Thakur, N., & Sharma, A. (2016). A review of supervised machine learning

540 algorithms. *3rd International Conference on Computing for Sustainable Global*
541 *Development (INDIACom)* (pp. 1310-1315). IEEE.

542 Taylor, R. (1990). Interpretation of the Correlation-Coefficient - a Basic Review. *Journal of*
543 *Diagnostic Medical Sonography*, 6(1), 35-39. doi:10.1177/875647939000600106.

544 Tishby, N., Pereira, F., & Bialek, W. (2000). The information bottleneck method. *arXiv preprint*
545 *physics/0004057*.

546 Trimble, S. W. (1999). Decreased rates of alluvial sediment storage in the Coon Creek Basin,
547 Wisconsin, 1975-93. *Science*, 285(5431), 1244-1246.

548 US Geological Survey. (2017). 1/3rd arc-second Digital Elevation Models (DEMs) - USGS
549 National Map 3DEP Downloadable Data Collection.

550 Verstraeten, G., Poesen, J., de Vente, J., & Koninckx, X. (2003). Sediment yield variability in
551 Spain: a quantitative and semiquantitative analysis using reservoir sedimentation rates.
552 *Geomorphology*, 50(4), 327-348.

553 Viger, R. J., & Bock, A. (2014). GIS features of the geospatial fabric for nation hydrologic
554 modeling. *US Geological Survey*. doi:https://doi.org/10.5066/F7542KMD

555 Vorosmarty, C., Meybeck, M., Fekete, B., Sharma, K., Green, P., & Syvitski, J. (2003).
556 Anthropogenic sediment retention: Major global impact from registered river
557 impoundments. *Global and Planetary Change*, 39, 169-190.

558 Xiang, Z., & Demir, I. (2020). Distributed long-term hourly streamflow prediction using deep
559 learning - A case study for State of Iowa. *Environmental Modelling & Software*, 131,
560 104761.

561 Xu, H., Demir, I., Koylu, C., & Muste, M. (2019). A web-based geovisual analytics platform

562 foridentifying potential contributors to culvert sedimentation. *Science of the Total*
563 *Environment*, 692, 806-817.

564 Zdaniuk, B. (2014). Ordinary Least Squares (OLS) Model. *Encyclopedia of Quality of Life and*
565 *Well-Being Research*. doi:http://dx.doi.org/10.1007/978-94-007-0753-5_2008

566 Zounemat-Kermani, M., Kisi, O., Piri, J., & Mahdavi-Meymand, A. (2019). Assessment of
567 artificial intelligence-based models and metaheuristic algorithms in modeling
568 evaporation. *Journal of Hydrologic Engineering*, 24(10), 04019033.

569 Zounemat-Kermani, M., Mahdavi-Meymand, A., Alizamir, M., Adarsh, S., & Yaseen, Z. (2020).
570 On the complexities of sediment load modeling using integrative machine learning:
571 Application of the great river of Loiza in Puerto Rico. *Journal of Hydrology*, 585,
572 124759.

573

574 **Table 1.** Recursive Feature Eliminated (RFE) ranked dataset variables

Index	Variable	Units Imperial (SI)	Metric Unit Conversion Factor	Calibrated Standard Scaled Data - OLS Coefficients	Calibrated Unscaled Data - OLS Coefficients
1	Basin Area	mi ² (km ²)	0.386	1.42	0.553
2	Initial Capacity	acre-ft (m ³)	8.11×10^{-4}	1.03	0.476
3	Cumulative Precipitation	in (mm)	3.93×10^{-2}	0.323	0.383
4	Hydraulic Length	ft (m)	3.28	-0.259	-0.181
5	Max Monthly Precipitation	in (mm)	3.93×10^{-2}	0.234	0.561
6	Curve Number	n/a	-	0.144	1.63
7	Total Upstream Dam Height	ft (m)	3.28	-0.119	-0.0494
8	Total Upstream Normal Storage	acre-ft (m ³)	8.11×10^{-4}	0.100	0.0250
9	Basin Relief	ft (m)	3.28	-0.0369	-0.0267
10	Channel Slope	ft/ft (m/m)	1.00	0.0226	1.91
11	Average Basin Latitude	°	-	0.0197	0.192
12	Mean Monthly Precipitation	in/mo. (mm/mo.)	3.93×10^{-2}	0.0158	0.0589

575
576 **Table 2.** Summary statistics for capacity loss models based on untransformed data

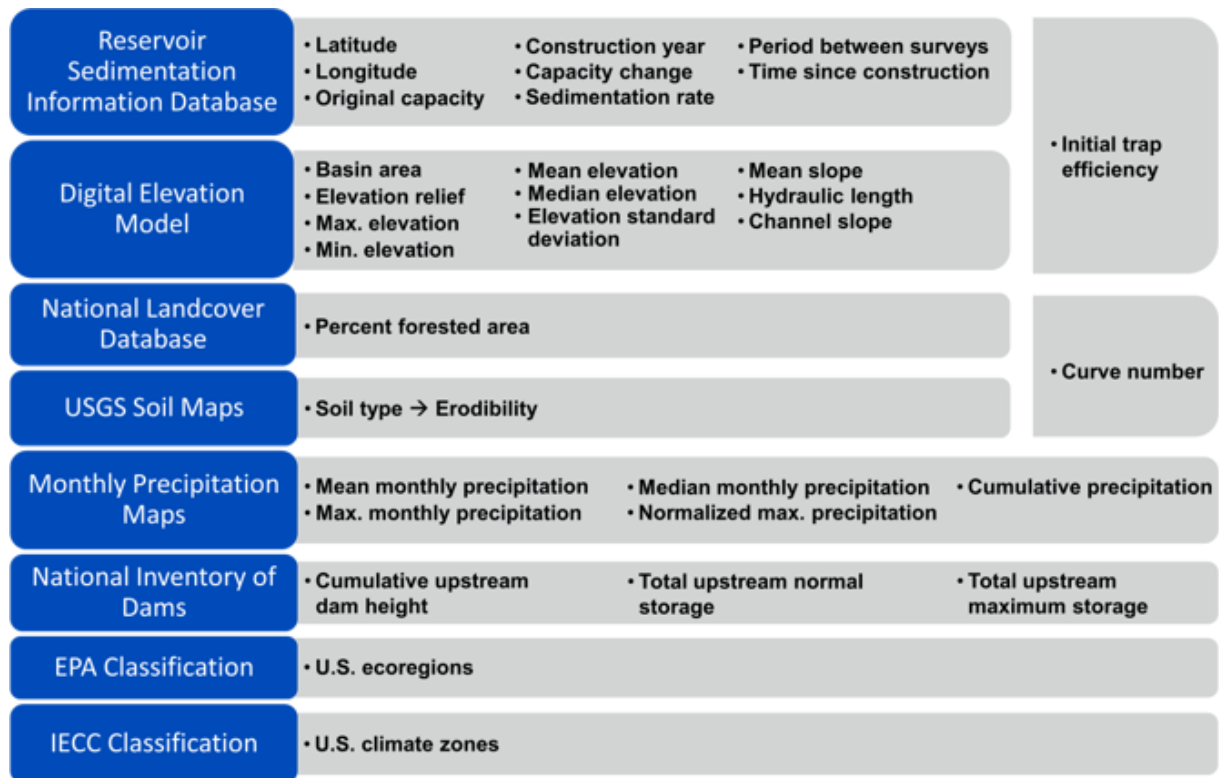
MODEL	Untransformed Statistics											
	Training						Testing					
	R ²	MAE	MAPE	RRMSE	RMSE	MSE	R ²	MAE	MAPE	RRMSE	RMSE	MSE
OLS	0.54	1.3E+07	220	155	3.6E+07	1.1E+12	0.36	3.2E+07	74	298	1.5E+08	1.9E+13
SVM	0.24	2.5E+07	165	323	1.2E+08	1.1E+13	0.38	1.7E+07	109	194	5.1E+07	2.1E+12
RFR	0.61	1.4E+07	40	232	8.2E+07	5.5E+12	0.57	1.4E+07	254	162	4.2E+07	1.5E+12
DTR	1.00	0	0	0	0	0	0.12	2.2E+07	1268	231	6.0E+07	3.0E+12
PLS	0.38	2.1E+07	211	294	1.0E+08	8.9E+12	0.53	1.4E+07	145	169	4.4E+07	1.6E+12
DNN _{P11}	0.83	1.4E+07	87	155	5.5E+07	2.5E+12	0.70	1.3E+07	295	135	3.5E+07	1.0E+12
DNN _{PD1}	0.72	2.3E+07	106	198	7.0E+07	4.0E+12	0.45	2.0E+07	327	182	4.8E+07	1.8E+12
DNN _{P12}	0.17	2.5E+07	187	339	1.2E+08	1.2E+13	0.35	1.7E+07	282	199	5.2E+07	2.2E+12
DNN _{PD2}	0.41	2.1E+07	189	287	1.0E+08	8.4E+12	0.39	1.6E+07	333	192	5.0E+07	2.0E+12
*Calib. OLS	0.40	1.9E+07	195	280	8.9E+07	6.4E+12	-	-	-	-	-	-

577

578 **Table 3.** Untransformed metrics. Highlighted cells indicate satisfactory metrics

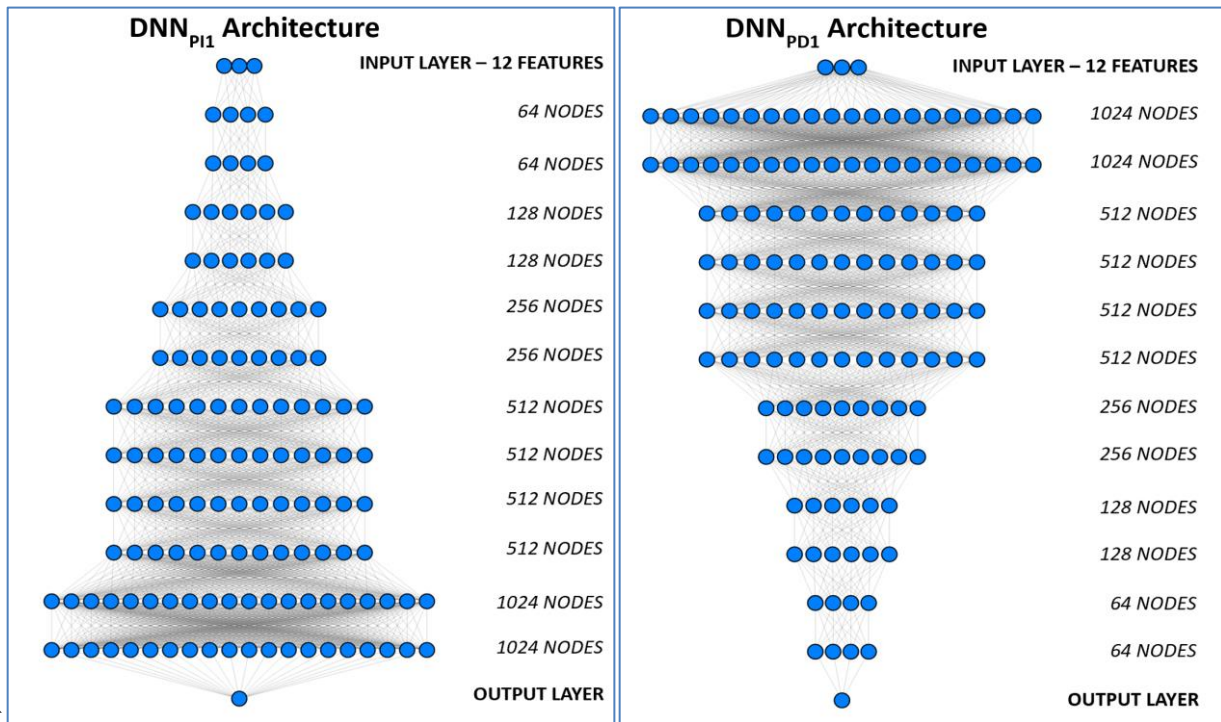
MODEL	Untransformed Statistics							
	Training				Testing			
	R ²	PBIAS(%)	RSR	r	R ²	PBIAS(%)	RSR	r
OLS	0.54	29.45	0.67	0.75	0.36	57.79	0.80	0.80
SVM	0.24	59.57	0.87	0.68	0.38	54.20	0.79	0.78
RFR	0.61	34.35	0.62	0.92	0.57	40.47	0.66	0.85
DTR	1.00	0	0	1.00	0.12	9.15	0.94	0.50
PLS	0.38	41.87	0.79	0.71	0.53	35.87	0.69	0.79
DNN _{PI1}	0.83	14.77	0.42	0.94	0.70	12.49	0.55	0.84
DNN _{PD1}	0.72	-32.77	0.53	0.88	0.45	-37.95	0.74	0.85
DNN _{PI2}	0.17	64.41	0.91	0.64	0.35	56.84	0.81	0.82
DNN _{PD2}	0.41	52.15	0.77	0.84	0.39	46.36	0.78	0.76
*Calib. OLS	0.40	39.03	0.78	0.71	-	-	-	-

579

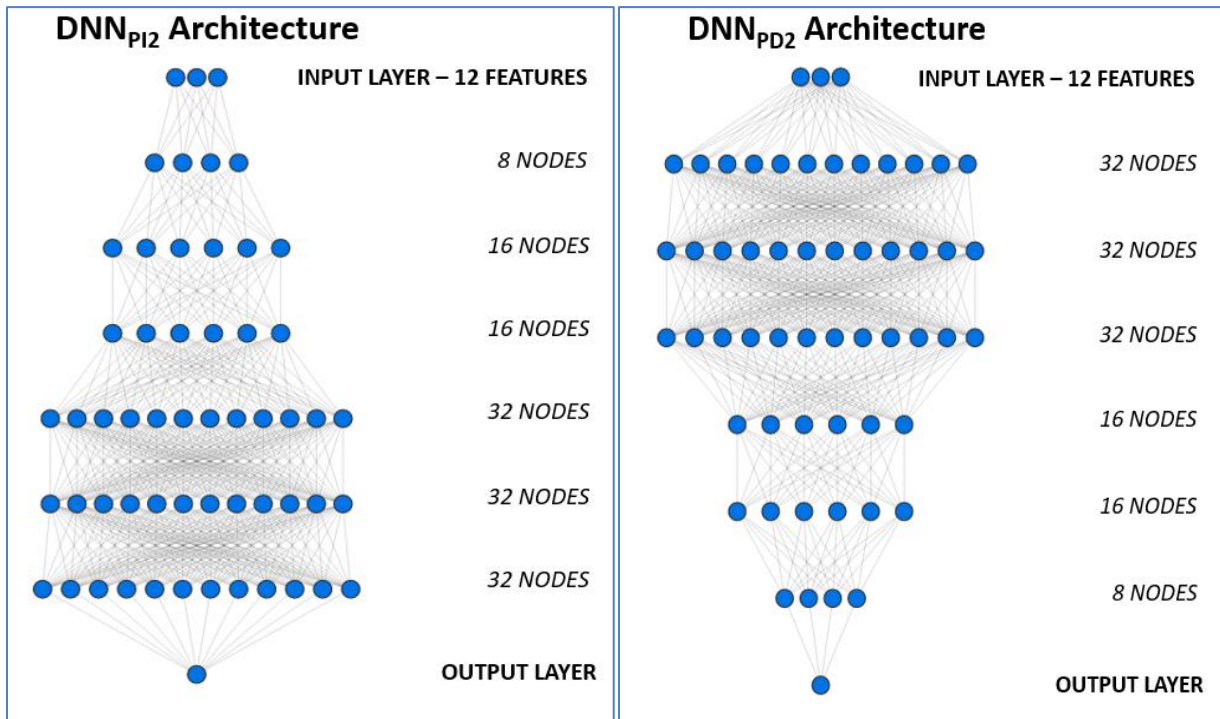


580

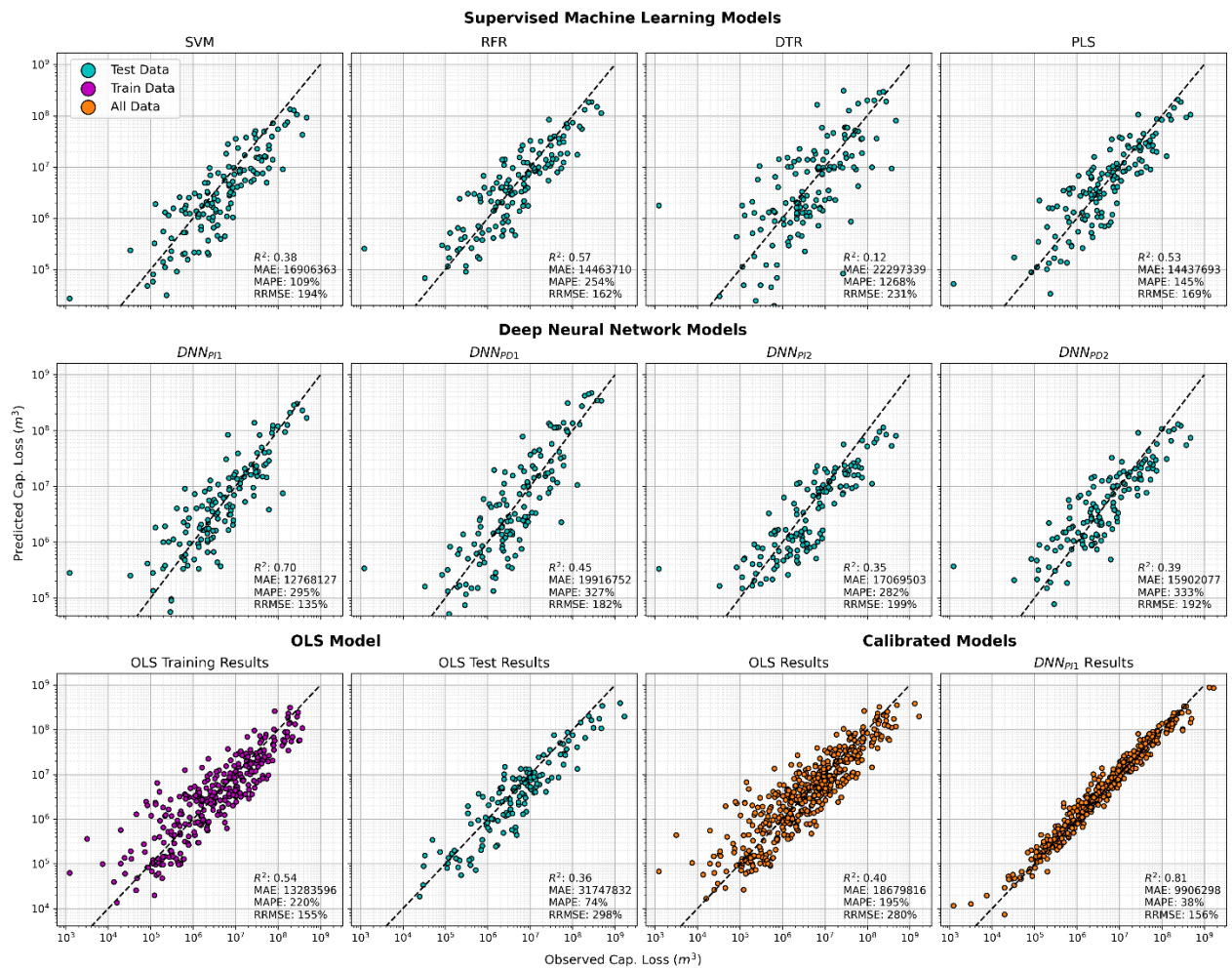
581 **Fig. 1.** Data sources and derived variables (numerical and categorical) of the composite RSI
 582 dataset. Variables in bold are time dependent



583
584 **Fig. 2.** Diagrams of the hidden-layer architectures of DNNPI1 (left) and DNNPD1 (right) with
585 the respective nodes present in each of their layers

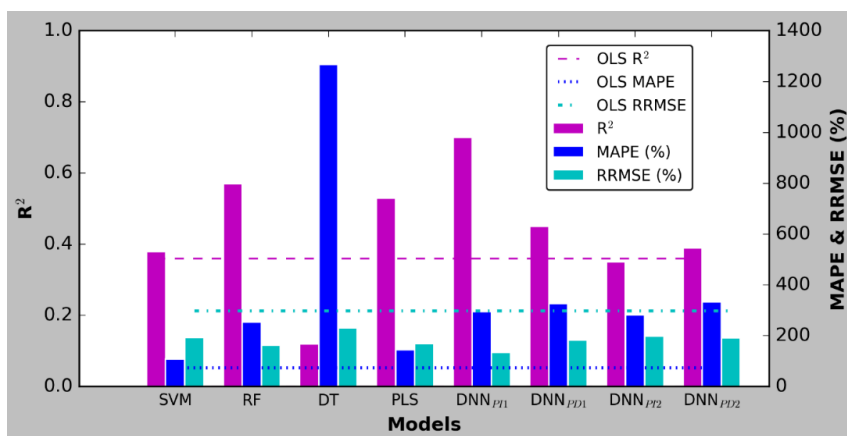


586
587 **Fig. 3.** Diagrams of the hidden layer architectures of DNNPI2 (left) and DNNPD2 (right) with
588 the respective nodes present in each of their layers



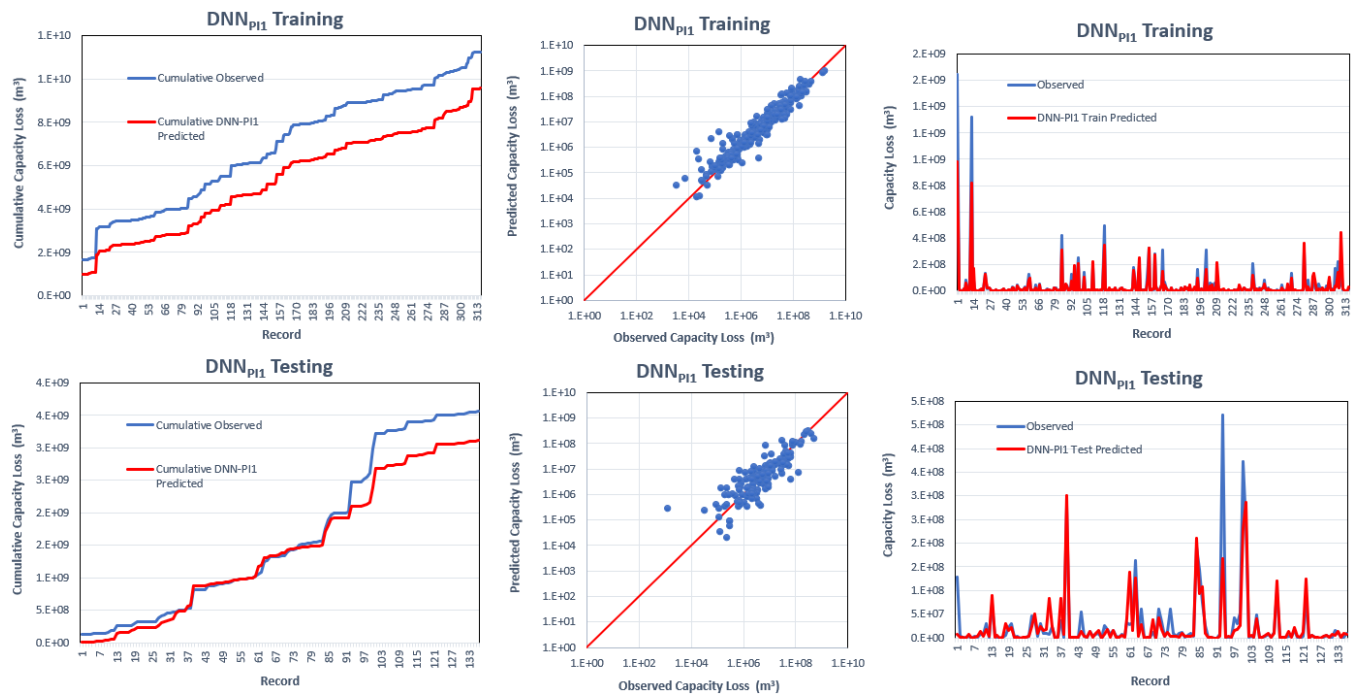
589
590

Fig. 4. Comparison of all predictive models



591
592
593

Fig. 5. Comparison of R^2 , MAPE, and RRMSE values across all models, related to the respective OLS method values



594
595
596

Fig. 6. Cumulative capacity loss, observed vs. simulated capacity loss, and capacity loss data series corresponding to the untransformed metrics for the DNN_{P11} machine learning model

597 **List of Table and Figure Captions**

598 **Table 1.** Recursive Feature Eliminated (RFE) ranked dataset variables

599 **Table 2.** Summary statistics for capacity loss models based on untransformed data

600 **Table 3.** Untransformed metrics. Highlighted cells indicate satisfactory metrics

601 **Fig. 1.** Data sources and derived variables (numerical and categorical) of the composite RSI
602 dataset. Variables in bold are time dependent

603 **Fig. 2.** Diagrams of the hidden-layer architectures of DNN_{PI1} (left) and DNN_{PD1} (right) with the
604 respective nodes present in each of their layers

605 **Fig. 3.** Diagrams of the hidden layer architectures of DNN_{PI2} (left) and DNN_{PD2} (right) with the
606 respective nodes present in each of their layers

607 **Fig. 4.** Comparison of all predictive models

608 **Fig. 5.** Comparison of R^2 , MAPE, and RRMSE values across all models, related to the respective
609 OLS method values

610 **Fig. 6.** Cumulative capacity loss, observed vs. simulated capacity loss, and capacity loss data series
611 corresponding to the untransformed metrics for the DNN_{PI1} machine learning model